Mapping Extended Structure with the Homogeneous ATA

Wm. J. Welch
Rick Forster
UC Berkeley

February 28, 2008

Abstract

The lack of large scale structure in correlator array maps is the result of the hole in the center of the visibility plane that arises because the smallest spacing between antennas is limited to one antenna diameter. Such a map has no total flux, for example. For extended surveys which use multiple pointings of the array antennas, the largest structures are totally missing. However, visibility data may be obtained for the region in the center of the hole in the visibility plane by adding a single antenna total power map. This can be accomplished by Fourier transforming the map and dividing out the transform of the gain function to produce the central visibilities. If a mosaic of pointings is obtained with the array in its interferometric mode, this data set allows extrapolation of the visibilities inward from the edge of the hole. This can be done by a procedure similar to that for the single dish in which the gain function is divided from the observed visibilities to obtain visibilities within the edge of the hole. From the overlap, a complete map may be constructed. Pointing errors spoil this procedure. The effect of the pointing errors is to produce phase and amplitude errors in the visibilities that increase toward the overlap region from both the origin and the edge of the hole. This is doubly bad, because the transforms of the gain functions also tend toward zero in the overlap region and dividing out the gain increases the data errors. For the homogeneous array, in which the single antenna total power contribution is from one or more of the array antennas in total power mode, the

effects of even small errors in pointing are significant. A study of the propagation of these errors shows that if pointing errors in both the total power observations and in the array observations do not exceed about 1/30 of an antenna beam, map accuracies of about 10% in all angular scales can be achieved.

For the total power observations, rapid comparison to a reference position on the sky will be important to insure that the measurement uncertainties are dominated by the system noise rather than by drifting system gain. For spectral line studies, it should suffice to intersperse five minute observations of a mosaic of pointings with five minute observations toward a reference sky direction. This would be done with the combined interferometric and autocorrelation observing. For continuum observing a different strategy is required because of the small system noise fluctuations relative to the system gain drifts on, say, the above five minute integrations. The mosaiced interfrometer maps must be augmented by observations made during rapid slewing of the antennas with short integration source sample times and a long reference source integration time during the slew turnaround. These observations would be done separately from the interferometric observation with all antennas observing together to provide a sensitive continuum map in a short time.

1 Introduction

Imaging of fields larger than the primary beam of the 6m ATA antenna will be important for much of the science that is planned. This means that a map will be made up from a mosaic of pointings of the array across the large field. For Nyquist sampling, the grid of pointings should be spaced by no more than one half primary beam width. Because the shortest array spacings are limited by the antenna diameter, visibility data obtained from the array is missing in the central part of the uv plane for all pointings. This is not a problem for studies of distributions of sources of diameters much smaller than the primary beam. However, regions with extended structures larger than the primary beam width will not have the large structures detected by the array. It requires the addition of map data from a single dish or from an array of smaller dishes. The latter option is not possible since such an array of smaller dishes is not available. The single dish fills in the central data best when its diameter is much larger than that of any of the array dishes.

That option is also not readily available. Larger antennas do exist, of course, but they typically don't have either the frequency agility of the ATA or the available time.

The autocorrelations at each 6m antenna as well as the crosscorrelations are recorded, and maps made with these autocorrelations can be used for the large scale structures. However, very good calibration and pointing accuracy are required for this procedure to work well.

2 Effect of Pointing Errors on Mosaic Images with a Homogeneous Array

One or more of the elements, operating in single antenna mode, can be used to add data into central the hole. The latter data are observed in the image plane, whereas the array data arrive in the visibility plane. The two planes are linearly related by the Fourier Transform. Let $T_B(x, y)$ be the brightness of the sky. (x, y) are the angular coordinates in the image plane, and $\mathrm{g}(x, y)$ is the antenna gain function. For a single pointing of the interferometer, the sky brightness is weighted by the antenna gain function, and we observe the visibility with the array

$$V(u, v) = \int_{-\infty}^{\infty} g(x, y) T_B(x, y) e^{-i2\pi(ux+vy)} dx dy \tag{1}$$

Suppose that $T_A(x, y)$ is a map of the source made with one of the antenna elements. Since $T_A(x, y)$ is a convolution of $T_B(x, y)$ with the antenna gain function, $T_A(x, y) = T_B(x, y) * \mathrm{g}(x, y)$, it can be Fourier transformed to $t_A(u, v) = \mathrm{G}(u, v)\mathrm{V}(u, v)$ in the (u, v) plane. To extract $\mathrm{V}(u, v)$, it is necessary to form effectively the fraction

$$V(u, v) = t_A(u, v)/G(u, v) \tag{2}$$

which works except where $G \to 0$. Since $\mathrm{g}(x, y)$ is typically close to a Gaussian function, $\mathrm{G}(u, v)$ is as well. Let Θ be the FWHM of the antenna with a circular beam and $\theta^2 = x^2 + y^2$.

$$g(\theta) \propto e^{-2.76(\theta/\Theta)^2} \tag{3}$$

Then G(u,v) has a similar form in terms of the radial visibility variable. $\beta = \sqrt{(u^2+v^2)}$

$$G(\beta) \propto e^{-3.58\Theta^2\beta^2} \tag{4}$$

The connection between Θ and D, the antenna diameter, is the usual diffraction formula.

$$\Theta = 1.2\lambda/D \tag{5}$$

Figure 1 shows the cross-section of the visibility plane near the origin. For single pointing of the array antennas, visibility is obtained only for $\beta \geq D/\lambda$. A plot of equation(3) in Figure 1 shows that $G(\beta) \rightarrow 0$ before β reaches D/λ. Thus, visibility data cannot be extracted from the single antenna observations all the way out to $\beta \sim D/\lambda$.

When we do a mosaic of pointings with the array to obtain an extended map, we get additional information about the large scales from the fact that we are observing each beam sized patch of the map with a sequence of different gain functions. Equation (1) now becomes a group of equations.

$$V(u,v;x_o,y_o) = \int_{-\infty}^{\infty} g(x-x_o, y-y_o)T_B(x,y)e^{-i2\pi(ux+vy)}dxdy \tag{6}$$

where (x_o, y_o) are the different pointing centers. This has the useful result that more information is obtained about the central visibility. (Ekers, and Rots, 1979; Cornwell, 1988). A transform of this data set made with respect to the mosaic of pointings (x_o, y_o) leads to the following formal result for the measured visibility.

$$FT[V(u,v;x_o,y_o)] = G^*(u_o,v_o)V(u+u_o, v+v_o), \tag{7}$$

where u_o and v_o are the variables in the transform from the mosaic pointings, x_o, y_o. The result is that there are measured visibility data off the ordinary u,v tracks at distances given by u_o, v_o, weighted by $G^*(u_o,v_o)$. Recovering visibilities from equation (7) requires the same kind of division that is implied by equation (2). Depending on the width of G(u,v), this data will overlap that which comes from the single dish measurements. For the homogeneous array, it is the same G(u,v) for both contributions, and this distribution is shown as another plot of equation (3) centered at the smallest value of β given by the array, D/λ, in Figure 1. The overlap is now significant and shows why the combination of single dish plus mosaic array data for the homogeneous array should give an image that is fully sampled and accurate at the short spacings. Simulations show that it works for perfect data. We have assumed here that the array antenna distribution has short spacings that provide visibility measurements close to the edge of the hole.

The presence of pointing errors spoils the image formation contributions of both the single antenna maps and the array visibility observations. It is useful to consider them separately.

2.1 The Visibility Errors from the Single Antenna

From the single antenna map, visibility data is extracted corresponding to values of u and v from 0 to $\leq D/\lambda$. In this data, the larger values of u and v correspond to greater separations of pairs of patches on the antenna. Figure 2 illustrates how phase errors in these visibilities arise if there are pointing errors. Figure 2 also suggests a way to evaluate the effects of the pointing errors. Begin with the explicit connection between $T_A(x,y)$ and its transform.

$$T_A(x,y) = \int_{-\infty}^{\infty} V(u,v)G(u,v)e^{i2\pi(ux+vy)}dudv \tag{8}$$

With pointing errors δx and δy,

$$T_A(x+\delta x, y+\delta y) = \int_{-\infty}^{\infty} V(u,v)[G(u,v)e^{i2\pi(u\delta x+v\delta y)}]e^{i2\pi(ux+vy)}dudv \tag{9}$$

The effective transfer function is now

$$G_{eff}(u,v) = G(u,v)e^{i2\pi(u\delta x+v\delta y)} \sim G(\beta)e^{i2\pi\beta\delta\theta} \tag{10}$$

G_{eff}(u,v) contains phase errors which will distort the Visibility V(u,v) derived from equation (1). The phase errors are greater for larger u and v for a given pointing error. The use of a radial cut in the uv plane with the radial variable $\beta = \sqrt{(u^2+v^2)}$ simplifies the discussion.

Consider two limiting cases. In the first, the errors change slowly, perhaps during a snap-shot observation, but are randomly distributed among the antennas with RMS expectation σ_θ. If the pointing error in the phase term of equation(9) is replaced by its expectation and β is set equal to sD/λ, where $0 \leq s \leq 1$, so that s is the radial variable of the hole normalized to one, then the typical phase error is

$$\Delta\phi = 2\pi\beta\sigma_\theta = 2\pi(sD/\lambda)\sigma_\theta = 2.4\pi s(\sigma_\theta/\Theta) \tag{11}$$

It is at the half radius, s=1/2, where the visibility data from the single dish measurements must overlap with those obtained from the array. For (σ_θ/Θ)=0.1, one tenth beamwidth pointing accuracy, $\Delta\Phi = .38(22^o)$ at this point. For (σ_θ/Θ)=.05, it is 0.19(11^o). These are large errors from small pointing errors. Perley (1989) notes that a 10^o phase error is equivalent to a visibility amplitude error of 20% in the construction of images.

In the other limiting case, the pointing errors vary rapidly at each antenna during the observations, perhaps due to the wind. In this case, the phase errors approximately average out to zero. However, there is a loss in amplitude due to the decorrelation caused by the fluctuating phase. If the fluctuations are normally distributed,

$$Expectation[e^{i\phi}] = e^{-\sigma_\phi^2/2} \tag{12}$$

From the discussion above, with σ_θ now corresponding to rapid fluctuations,

$$\sigma_\phi^2 = (2.4\pi s\sigma_\theta/\Theta)^2 \tag{13}$$

and the loss of amplitude is by the following factor.

$$e^{-1/2(2.4\pi s\sigma_\theta/\Theta)^2} \tag{14}$$

At the mid radial point, s=1/2, this factor is 0.93 for σ_θ/Θ=0.1. The functional form of this error factor is a Gaussian just like the basic function $G(\beta)$ in equation (4). Including this factor in equation(4) leads to a narrower and uncertain composite Gaussian. Altogether, the effective overlap region is reduced as well as the visibility data being made uncertain.

2.2 Visibility Errors from Scanning the Array Antennas(Mosaicing)

Equation (7) above is the result of a transform of the visibility data from the array with respect to the mosaic of pointings, x_o, y_o. The effect of the multiple pointings is to provide interferometer visibilities with the set of gain functions $g(x - x_o, y - y_o)$. That is, we get a different interferometric image from each pointing. The effect of pointing errors on these observations can be found starting with the inverse transform of $g(x - x_o, y - y_o)$.

$$g(x - x_o, y - y_o) = \int_{-\infty}^{\infty} G(u, v)e^{i2\pi[u(x-x_o)+v(y-y_o)]}dudv \tag{15}$$

With pointing errors δx and δy in x_o and y_0 respectively,

$$g(x - x_o - \delta x, y - y_o - \delta y) = \int_{-\infty}^{\infty} [G(u,v)e^{-i2\pi(u\delta x + v\delta y)}]e^{i2\pi[u(x-x_o)+(y-y_o)]}dudv \tag{16}$$

Just as in equation(9) above, the pointing errors in the array give rise to an erroneous effective $G_{eff}(u,v)$ which is $G(u,v)$ with the additional factor $e^{-i2\pi(u\delta x + v\delta y)}$. All the relations worked out above apply in this case as well. Both the phase errors and amplitude errors increase with distance u_o and v_o away from the regular uv track. In particular, the data extrapolation inward from the edge of the hole is more uncertain the farther it is carried.

It is clear how the image fidelity and dynamic range are degraded by the pointing errors for the homogeneous array. Where the two data sets overlap at the half diameter radius of the hole, they spoil the inter-comparison, so that the good mutual calibration of the data sets is degraded. In addition, because the weighting by the gain transfer function at the half radius point is only $\leq .25$ of what it is elsewhere, the errors are multiplied up in the inversion process. In principle, single dish maps with about three single antennas should provide adequate signal/noise for the combination of data to have adequate signal/noise. This is because the short spacing visibility data has the largest intensity. In the case of the ATA-42 there are just three short spacing pairs. However, in view of the uncertainties in the observations, it would be wise to obtain single dish maps from at least a dozen or so antennas and combine them. This will somewhat reduce the uncertainties in the final maps. In fact, it would probably be best to use all of the antennas in single dish mode to get the best results.

If we combine the effects of pointing errors in both the single antenna total power observations and the interferometric observations, we find that **in order to have brightness errors in the final composite maps that are no worse than 10% we must have pointing errors no worse than about 1/30 of a beamwidth for both modes of observing.**

Tests done at the VLA at cm wavelengths (Cornwell, T. 1988, A&A, 202, 316.) indicate that combining array data with total power data from the array antennas does work, and at mm wavelengths in the CO(1-0) line, Marc Pound made a good map of the Eagle Nebula combining a Mosaic interferometer map made with the BIMA array and a single antenna map made with the Bell Labs 7m antenna (Pound, 1998, ApJ, 493L, 113).

3 Total Power Observing

Apart from the tight pointing requirements for the large scale mapping, the other big problem is obtaining the total power map without a rapid comparison system. Classical single antenna observing is done with a rapid comparison switch (a Dicke switch) at the input. Whereas the interferometer observing should have no offsets, a total power measurement is made on top of the system temperature, and gain drifts in time produce varying offsets. For the ATA antenna, there is no input switch at the receiver input for simplicity, and there is no obvious way to introduce a chopping mirror in the optics. That leaves the need to follow a total power measurement with one toward a reference direction in a time short compared with the time interval of significant gain drifts.

For a radiometer with system temperature T_{sys}, RF bandwidth B, and integration time τ, the fractional output RMS fluctuations referred to the input are the familiar $\frac{\Delta T}{T_{sys}} = \frac{2}{\sqrt{B\tau}}$. If the input is perfectly balanced with a rapid switch to a reference load, one should achieve that sensitivity. The switching time must be short compared with the time for significant gain variations to occur. If there is no switch, then the gain variation may dominate. If the gain were G and it varied by an amount ΔG, then the output fluctuations referred to the input would have $\frac{\Delta T}{T_{sys}} = \frac{\Delta G}{G}$. Gain variations grow with time, whereas the basic measurement fluctuations decrease with time. A short comparison time must be used. The basic parameters are evidently receiver bandwidth and integration time τ and the gain variation during the measurement time τ.

We made gain fluctuation measurements on one of the ATA antenna systems, that of antenna 3H, which we assume is typical. For the first set of measurements, we placed a large piece of absorber in front of the feed that terminated it pretty well for most frequencies. Then we measured the output power fluctuations at the antialiasing filtered analog output of one channel in the RFCB. We tuned the channel, of width 200 MHz, successively to bands from one to ten GHz. Bands at frequencies above five GHz usually have little interference. Then we took output records from an HP power meter integrated over one second intervals and recorded them. Figure 3 shows results for short times, up to 10 minutes, for all the bands. Some incidences of interference are evident in the lower frequency bands, but the results are similar at all the bands. For times of one to three minutes, the

RMS fluctuations are on the order of 2 $\times 10^{-4}$ for all of the bands. For times of the order of 10 minutes, they are closer to 10^{-3}, or a little more. For one minute the stability is good. We then made a very long integration, more than 15 hours to see what the long term stability is like. This is shown in Figure 4. The average remains constant to a few percent. For this plot, the antenna was pointed at a fixed direction to the North at a elevation of 30^o, and there was no absorber. The weather was clear, and we had some evidence that the load produced a slightly quieter result, by a factor of about 2, as compared with the background on the sky. What is striking in this plot is that the output is periodic. Comparison with earlier temperature records for the electronics room, showed that the period was the same as that of the room temperature, 10 to 20 minutes. This is the period of the room air conditioner.

We made one further measurement which was to remove the RFCB and just look at the sky with a diode detector on the wide band fiber cable coming into the electronics room. This is shown in Figure 5. In this case the total input band of 0.5 -12 GHz on the cable is being detected. Sharp spikes that are probably interference are evident. Between the spikes the gain is stable to about 1.6×10^{-3} over an hour which is smaller than at the output of the RFCB by a factor of three. Encasing the RFCB chassis in foam insulation to give it a longer time constant could possibly remove that factor of three.

4 Observing strategies

The goal is to have the output fluctuations dominated by the basic radiometer fluctuations rather than the gain fluctuations. During a mosaic of pointings to obtain a large map, the autocorrelations for each antenna are recorded as well as the cross-correlations. The simplest scheme would be just to combine the autocorrelations for all the antennas to obtain the map for the large scale and then add it to the cross-correlation image. The main problem will be the drifting total power offsets in the autocorrelation maps. Averaging over all the single antenna maps might help average out some of the drifting. On the other hand, the measurements discussed above suggest that the drifts will be common. Table 1 below shows how the electronic noise, $\frac{2}{\sqrt{B\tau}}$, depends on the expected bandwidths and integration times.

B - τ	2.5 second	60 second	5 minutes
100 MHz	1.3 $\times 10^{-4}$	2.5 $\times 10^{-5}$	1.1 $\times 10^{-5}$
100 kHz	4.0 $\times 10^{-3}$	8.0 $\times 10^{-4}$	4.0 $\times 10^{-4}$
10 kHz	1.3 $\times 10^{-2}$	2.6 $\times 10^{-3}$	1.2 $\times 10^{-3}$
3 kHz	2.3 $\times 10^{-2}$	5.0 $\times 10^{-3}$	2.2 $\times 10^{-3}$
1 kHz	4.0 $\times 10^{-2}$	8.0 $\times 10^{-3}$	3.6 $\times 10^{-3}$

The first row corresponds to the continuum bandwidth. The others are for the separate channels in spectral line observing with different overall correlator bandwidth settings. Since the correlator has 1000 channels, the second row is the individual channel width for the full correlator bandwidth. It provides a channel width of 20 km/sec for HI. The next row, 10 kHz, is 2 km/sec at HI which is close to the typical thermal width of 100K galactic HI. The next width, 1 kHz, is close to what might be useful for HI Zeeman line observing, thermal OH, or long chain molecules like HC_5N at, say, 5 GHz.

Table 3 summarizes the fractional gain fluctuations during different time intervals.

τ	$\frac{\Delta G}{G}$
1-3 min	2 $\times 10^{-4}$
5-10 min	2 $\times 10^{-3}$
60 min	5 $\times 10^{-3}$

The last entry for the 60 min case could be lowered to 1.6 $\times 10^{-3}$ if the observed effects of the periodic temperature changes in the electronics room could be eliminated as discussed above.

Consider the spectral line observing first. The 100 kHz filters will mostly only be used for extragalactic HI. Since most galaxies have some tilt with respect to the line of sight, there usually will be a velocity gradient across the galaxy that will make the source size small in each spectral channel. That makes the large scale imaging somewhat easier, even for large galaxies like M31. The interferometer image in each channel is mostly complete, but its level with respect to zero will not be correct unless total power data is added. To get the brightness scaled correctly if no single dish data is added, one should put a box around each feature and measure the brightness with respect to the nearby surroundings. This is the same step that one takes to get the fluxes of point continuum sources, where one fits a synthesized beam to each source to get its final flux.

10 kHz filters provide a resolution of 2 km/sec, the thermal line width for

galactic HI at 100K, and are too wide for many other constituents, except HI recombination lines. 1kHz may be the most useful. That's 0.2 km/sec for HI, about 0.3 km/sec for OH (close to the thermal width at 30K), and about 1/2 the thermal line width for the HC_5N line at 5 GHz. If we integrate for 30 minutes with the 1 kHz filters, the fractional thermal noise becomes 1.5×10^{-3}, comparable to or somewhat less than the fractional gain noise of the system, if the periodic room temperature fluctuation effects are removed. It is possible that adding up the maps from all of the antennas will average out some of this gain variation, but the part from the room temperature variation may be common. In any case, the thermal noise part should also average out, leaving the gain variation effects to dominate. This argues that a comparison spectrum needs to be taken after no more than about five minutes. One simple way to accomplish this would be to point the whole array toward an off position every five minutes for about five minutes during the mosaic scanning of the array and subtract the off spectra for each antenna auto correlation spectrum. Other similar schemes might be developed depending on the particular spectral line being observed. The overall spectral band of the spectrometer is narrow enough that it is unlikely that more than one spectral line will be observed at a time. The 1000 channels that are observing the line are very many, and it would make the most sense to over-resolve and then combine channels for better signal/noise later.

The continuum mapping at 100MHz bandwidth presents more of a problem. Table 1 shows that a 60 second integration with a bandwidth of 100MHz has a fractional RMS thermal noise of 2.5×10^{-5}, much smaller than any fractional gain variations on a scale of more than a minute. Since we have no rapid Dicke switch or chopping mirror, we need to use something like On The Fly mapping (OTF) (Emerson, Klein, and Haslam, 1979, A&A, 76, 92) to produce the large scale maps.

5 OTF Mapping

The basic idea is that a single antenna raster scan of the object under study will be made with a relatively rapid turn-around of the scan at the end of each row in a region that is off the source. During the scan across the source, the receiver power is read out at a rate which corresponds to at least the Nyquist sampling of the source structure. That is, at least as often as twice per beam width. Suppose, for example, that there are ten 2.5 second "on" observations across the source with a 25 second "off" observation at the end of each row. Each "on" observation is compared to the "off" at the turnaround, and so its thermal noise uncertainty is the 1.3 $\times 10^{-4}$ from table 1. The gain uncertainty should be about half the 2 $\times 10^{-4}$ listed in the first column of table 2, that is, about the same as the thermal noise. Reducing the sample time by a factor of two or more should make it relatively smaller. This example is appropriate for a 1 GHz observation with the scanning proceeding at 0.6 degrees/second. At 10 GHz, where the beamwidth is 10 times smaller, we would get the same times with a much slower scan rate, .06 degrees per second. These numbers are practical and represent a way of getting the large scale map with little degradation in sensitivity. For this mode, the scanning to get the large scale map must be done separately from the interferometric observing. Doing it on all of the antennas simultaneously and averaging the results will provide an accurate resulting summed map.

6 Constructing the Map

In principle, one could take the visibilities, V(u,v), found from the single dish data as discussed above, add them to the visibilities found from the cross correlations, and get the final map from the Fourier Transform. In practice, it will work better to combine the two data sets using the MOSMEM program (Stanimirovic et al, 1999) in Miriad, which produces combined images of all the channel maps from a joint maximum entropy deconvolution.

7 Summary

The major systematic inaccuracy of the single dish mode will be due to differential spillover in the "on" - "off" comparison. It is difficult to know in advance how much the reference pointing or the OTF scanning schemes will be plagued by this. The antenna background is of the order of 12K. The modulation of this by the scanning across the ground can only be determined by experiment. It is likely to be of the order of 1% of the expected background for small scans, that is, of the order of 0.1K. Averaging the offset or scanning observations over all of the antennas should further reduce this systematic error.

8 References

1. Sargent, A. I., and Welch, W. J. 1993, ARAA, 31. 297.

2. Perley, R. A., 1989, ASP Conference Series, no. 6, 287.

3. Ekers, R. D., and Rots, A. H., 1979, Proc. IAU Coll 49, Reidel, 61.

4. Cornwell, T. J., 1988, A &A, 202, 316.

5. Kogan, L. 1998, MMA Memo 217.

6. Stanimirovic, et al. 1999, MNRAS,, 302,417.

7. Pound, M. 1998,ApJ, 493L,113.

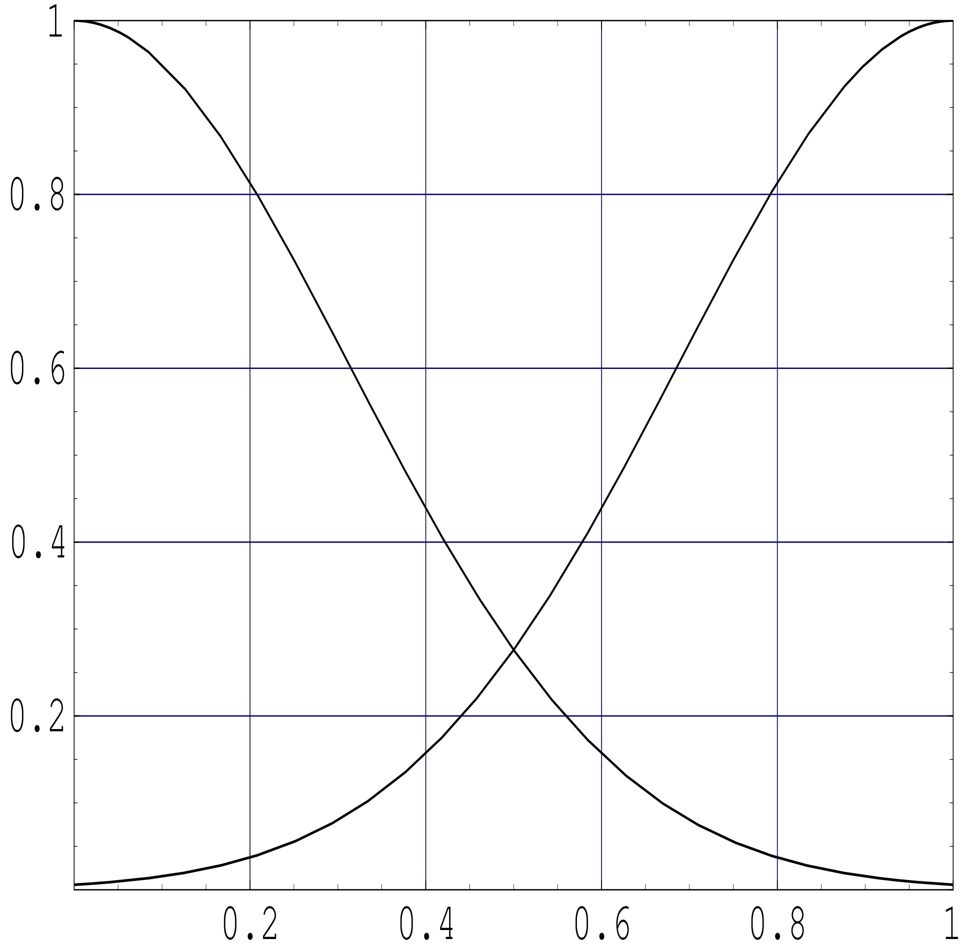

Figure 1: Transfer functions for the homogeneous array. The abscissa is the radial variable in the visibility plane normalized to D/λ, where D is the antenna diameter. The curve predominately on the left is the transform of the antenna gain function. The curve predominately on the right is the function which weights the extrapolation of visibility from the array multi pointing observations. It is the same function, except that it is centered at $\beta = D/\lambda$ and reverse imaged.

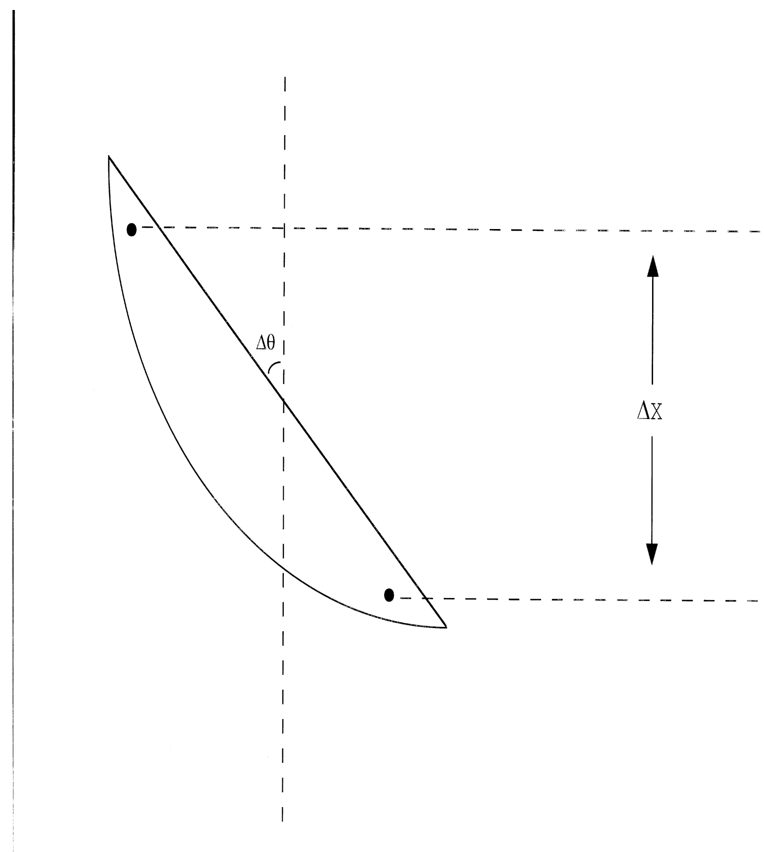

Figure 2: Sketch of an antenna with a pointing error. Lines to two patches on the reflector are shown. Visibilities corresponding to this separation, Δx, suffer a phase error of $(2\pi/\lambda)\Delta x\Delta\theta$.

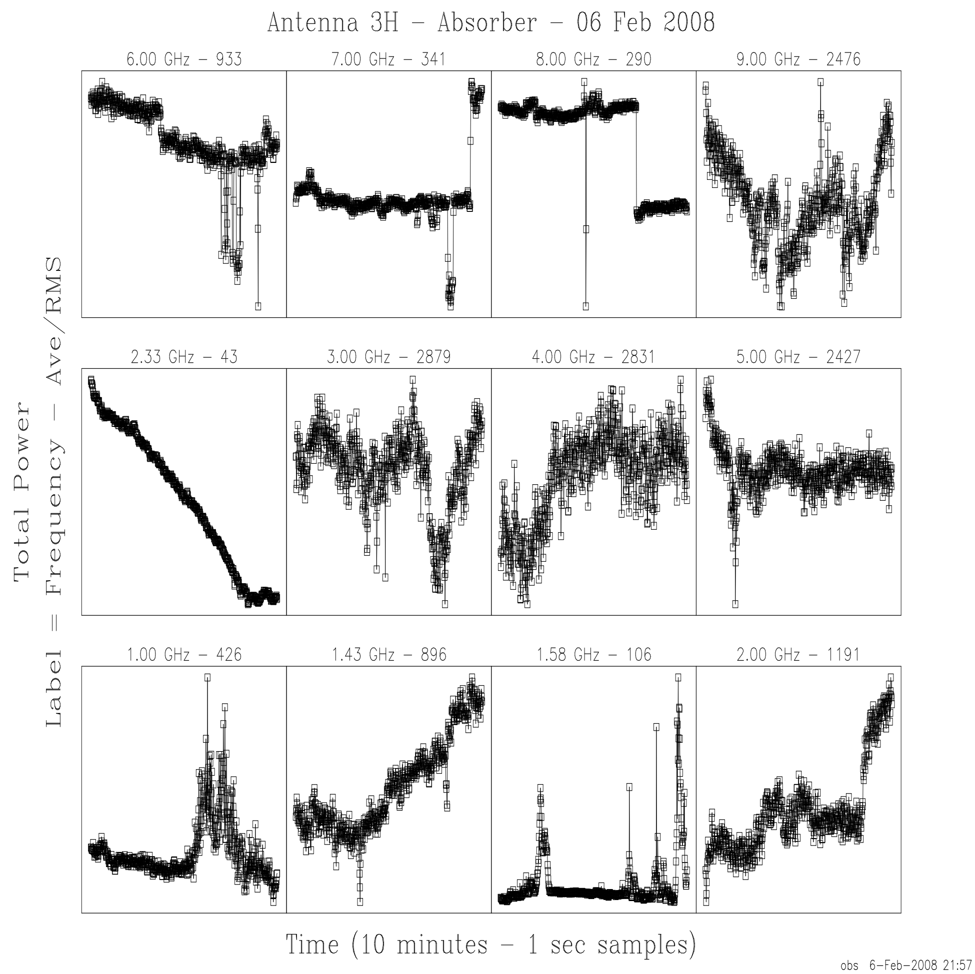

Figure 3: Total power measurements of the RFCB output for antenna 3H at 12 frequencies ranging from 1 GHz to 9 GHz over ten minutes in one second averages. The one for 2.33 Ghz shows interference from the XM satellite even past the absorbing load. Average/RMS is plotted for the whole ten minutes above and to the right for each panel.

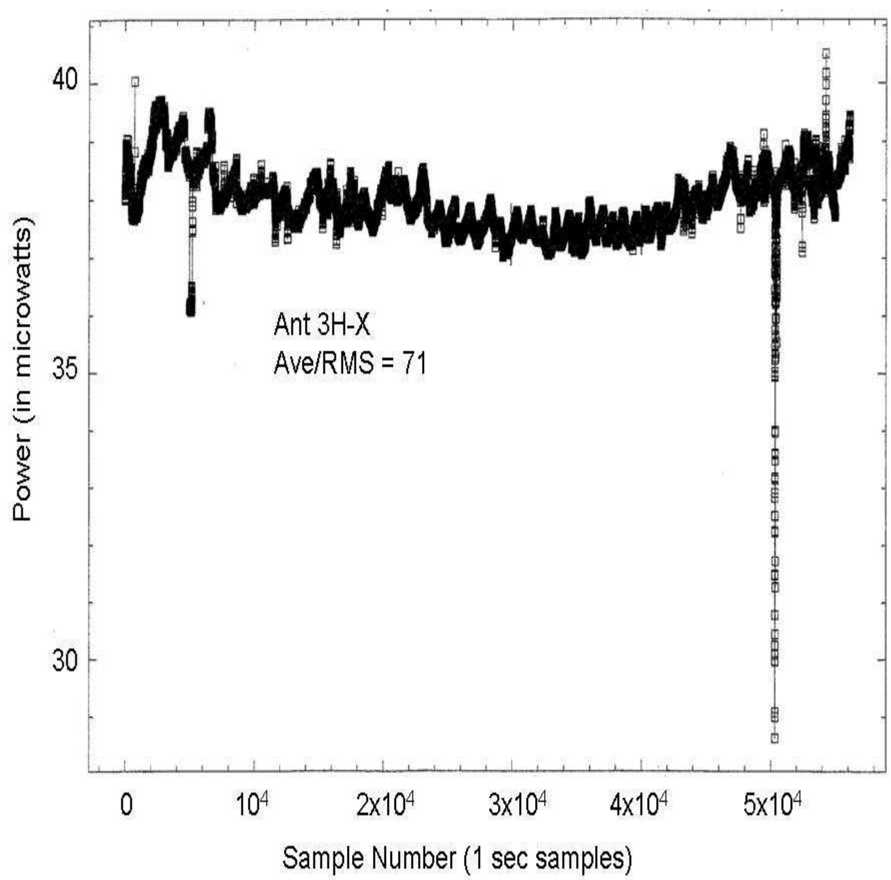

Figure 4: Total power measurements of the RFCB output for antenna 3H at 5.5GHz over 22 hours in one second averages. Variations at periods of 10 - 20 minutes, the period of the electronics room air conditioner, are evident.

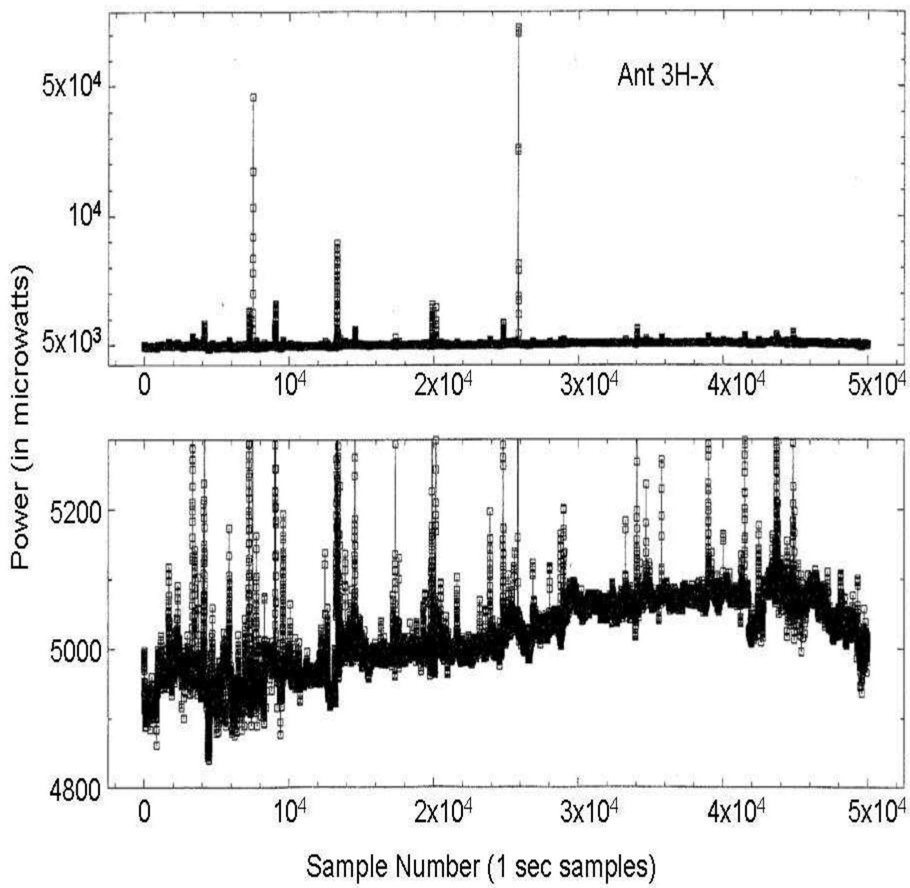

Figure 5: Total power measurements at just the diode detector in the lab following the optical fiber for antenna 3H. The entire 0.5 GHz to 12 GHz optical fiber band is present. The spikes are likely to be interference. The RMS fluctuations between the spikes are 1.6×10^{-3} for up to an hour.